Effect of chemical composition on the electrical conductivity of gneiss at high temperatures and pressures

Lidong Dai[1,*], Wenqing Sun[1,2], Heping Li[1], Haiying Hu[1], Lei Wu[1], and Jianjun Jiang[1]

[1]Key Laboratory of High-Temperature and High-Pressure Study of the Earth's Interior, Institute of Geochemistry, Chinese Academy of Sciences, Guiyang, 550081, China

[2]University of Chinese Academy of Sciences, Beijing, 100049, China

Correspondence to: Lidong Dai (dailidong@vip.gyig.ac.cn)

Abstract. Electrical conductivity of gneiss samples with different chemical compositions (W_A=Na_2O+K_2O+CaO=7.12%, 7.27% and 7.64% weight percent) were measured using a complex impedance spectroscopic technique at 623–1073 K and 1.5 GPa and a frequency range of 10^{-1} to 10^6 Hz. Simultaneously, a pressure effect on the electrical conductivity was also determined for the W_A=7.12% gneiss. The results indicated that the gneiss conductivities markedly increase with total alkali and calcium ion content. The sample conductivity and temperature conform to an Arrhenius relationship within a certain temperature range. The influence of pressure on gneiss conductivity is weaker than temperature, although conductivity still increases with pressure. According to various ranges of activation enthalpy (0.35–0.52 eV and 0.76–0.87 eV) at 1.5 GPa, two main conduction mechanisms are suggested that dominate the electrical conductivity of gneiss: impurity conduction in the lower temperature region and ionic conduction (charge carriers are K^+, Na^+ and Ca^{2+}) in the higher temperature region. The electrical conductivity of gneiss with various chemical compositions cannot be used to interpret the high conductivity anomalies in the Dabie–Sulu ultrahigh pressure metamorphic belt. However, the conductivity–depth profiles for gneiss may provide an important constraint on the interpretation of field magnetotelluric conductivity results in the regional metamorphic belt.

1 Introduction

According to magnetotelluric (MT) and geomagnetic depth sounding results, electrical conductivity of geological samples at high temperature and pressure can be used to extrapolate the mineralogical composition and thermodynamic state in the Earth's interior (Maumus et al., 2005; Dai et al., 2008; Hui et al., 2015; Manthilake et al., 2015; Li et al., 2016; Hu et al., 2017). High conductivity anomalies are widely distributed in the middle to lower crust and upper mantle, and there are various causes of these anomalies in different regions (Xiao et al., 2007, 2011; Pape et al., 2015; Novella et al., 2017). Hence, it is crucial to comprehensively measure the electrical conductivities of minerals and rocks that are distributed in the deep Earth. A series of electrical conductivity results of the main minerals and rocks have been reported in previous studies under high temperature and pressure conditions (Fuji-ta et al., 2007; Hu et al., 2011, 2013; Dai et al., 2012; Yang et al., 2012; Sun et al., 2017a). However, electrical conductivity of most metamorphic rocks have not been explored at high temperature and pressure, and thus the interpretation of high conductivity anomalies distributed in representative regional metamorphic belts is still not comprehensive.

A regional metamorphic ultrahigh pressure belt for the Dabie–Sulu orogen is a complexly giant geotectonic unit in central-eastern China. Geophysical exploration results confirmed that a large number of high conductivity anomalies have been observed in metamorphic belts (Xiao et al., 2007; Wannamaker et al., 2009; Zeng et al., 2015). Metamorphic rocks (e.g., slate, schist, gneiss, granulite and eclogite) with different degrees of metamorphism play an important role because of their widespread distribution in regional metamorphic belts. Dai et al. (2016) measured the electrical conductivity of dry eclogite at 873–1173 K, 1.0–3.0 GPa and different oxygen partial pressures (using Cu+CuO, Ni+NiO and Mo+MoO_2 solid oxygen buffers), and found that the hopping of small polaron is the dominant conduction mechanism for dry eclogite at high temperature and pressure. The electrical conductivity of natural eclogite is much lower than the high conductivity anomaly in the Dabie–Sulu ultrahigh pressure

metamorphic (UHPM) belt of eastern China. Granulite is another important metamorphic rock distributed in a majority of regional metamorphic belts. The electrical conductivity of granulite is lowered by repetitive heating cycles with a conductivity range about 10^{-7}–10^{-2} S/m at 1.0 GPa and up to about 900 K (Fuji-ta et al., 2004). Due to the complicated mineralogical assemblage of granulite and rock structure, the features of the electrical conductivity values over heating cycles have not been explained, and the conduction mechanism for granulite not definitively stated. Gneiss is formed at middle to lower crustal pressure and temperature conditions, and widely distributed in regional metamorphic belts. The main rock-forming minerals of gneiss are feldspar, quartz and biotite. The electrical conductivity of gneiss increases with temperature, and the conductivity values range from about 10^{-4}–10^{-2} S/m at up to 1000 K and 1.0 GPa (Fuji-ta et al., 2007). On the basis of the dominant rock-bearing mineralogical assembly of the metamorphic rock, gneiss can generally be divided into types, such as plagioclase gneiss, quartz gneiss and biotite gneiss. Therefore, it is crucial to investigate the electrical conductivity of gneisses with various chemical compositions and mineralogical constituents. The electrical conductivity of granite dramatically increases with alkaline and calcium ion content at 623–1173 K and 0.5–1.5 GPa (Dai et al., 2014). Impurity conduction has been proposed to be the dominant conduction mechanism for granite in the lower temperature region, and alkaline ions, including K^+, Na^+ and Ca^{2+}, are probable charge carriers at higher temperatures.

In the present study, we measured the electrical conductivity of gneiss samples in situ under 0.5–2.0 GPa, 623–1073 K and three different chemical compositions. The influences of temperature, pressure and chemical composition on the gneiss electrical conductivity were determined, and the dominant conduction mechanism for gneiss is discussed in detail. On the basis of the conductivity results, the geophysical implications for the high conductivity anomalies of the Dabie–Sulu UHPM belt were explored in depth.

2 Experimental procedures

2.1 Sample preparation

Three relatively homogeneous natural gneiss samples with parallel to foliation direction were collected from Xinjiang, China. The sample surfaces were fresh, non-fractured and non-oxidized, without evidence of alteration before and after the experiments. To determine the gneiss mineralogical assemblage, we used optical microscopy and scanning electron microscopy (SEM) at the State Key Laboratory of Ore Deposit Geochemistry, Institute of Geochemistry, Chinese Academy of Sciences, Guiyang, China. The major elemental content of the gneiss samples was analyzed by X-ray fluorescence spectrometry (XRF) at Australian Laboratory Services, Shanghai, China. The main rock-forming minerals of three gneiss samples were feldspar, quartz and biotite (Fig. 1). The volume percentage varied for each corresponding rock-forming mineral in different gneiss samples (Table 1). Three gneiss samples had the same mineralogical assemblage, and all of them belong to the biotite-bearing felsic gneiss. Table 2 shows the results of whole rock analysis by XRF for the three gneiss samples. We found that the total alkali, such as K^+ and Na^+, and the divalent cationic calcium metal ion content varied for each sample (Table 2).

2.2 Impedance measurements

High temperatures and pressures for the experiments were generated in a YJ-3000t multi-anvil apparatus, and the impedance spectra were collected using a Solartron-1260 impedance/gain-phase analyzer at the Key Laboratory of High-Temperature and High-Pressure Study of the Earth's Interior, Institute of Geochemistry, Chinese Academy of Sciences, Guiyang, China. All components of the experimental assemblage (ceramic tubes, pyrophyllite, Al_2O_3 and MgO sleeves) were previously baked at 1073 K for 12 h in a muffle furnace to avoid the influence of absorbed water on the electrical conductivity measurements. The sample was then loaded into a MgO insulation tube

(Fig. 2). Two nickel disks (6.0 mm in diameter and 0.5 mm in thickness) were applied to the top and bottom of sample to act as electrodes. To shield against external electromagnetic and spurious signal interference, a layer of nickel foil with a thickness of 0.025 mm was installed between the alumina and magnesia sleeves. These sleeves have good insulating properties for current and transmitting pressure. A pyrophyllite cube (edge length: 32.5 mm) was used as the pressure medium, and the heater was composed of three-layer stainless steel sheets with a total thickness of 0.5 mm. The sample assembly was placed in an oven at 330 K to keep it dry before the experiment.

In the experiments, the pressure was slowly increased to the desired value at a rate of 1.0 GPa/h, and then the temperature was increased at a rate of 300 K/h to the designated values. The Solartron-1260 impedance/gain-phase analyzer with an applied voltage of 3 V and frequency range of 10^{-1}–10^{6} Hz was used to collect impedance spectra when the pressure and temperature were stable. At the desired pressure, the spectra were measured at a certain temperature, which was changed in 50 K intervals. The impedance spectra of gneiss samples with W_A (Na_2O+K_2O+CaO)=7.12% were collected under conditions of 0.5–2.0 GPa and 623–1073 K. The spectra of the other two gneiss samples (W_A=7.27% and 7.64%) were measured at 623–1073 K and 1.5 GPa. To confirm the data reproducibility, we measured the electrical conductivity of gneiss over two heating and cooling cycles at a constant pressure. The errors of temperature and pressure were ±5 K and ±0.1 GPa, respectively.

3 Results

The typical complex impedance spectra for the run DS12 gneiss samples at 1.5 GPa and 623–1073 K are shown in Figure 3. All of these obtained spectra are composed of an almost ideal semicircle in the high frequency domain and an additional tail in the lower frequency domain. Other complex impedance spectra of the gneiss samples at other pressures displayed the same characteristics of those shown in Figure 3. Figure 4 displays the real and imaginary parts of complex impedance for the runs DS13 and DS14 gneiss samples as a function of the measured frequency at 1.5 GPa and 623–1073

K. The real part values almost remain unchanged over a frequency range of 10^6–10^4 Hz, and sharply increased at 10^4–10^2 Hz; these values then slowly increased within the 10^2 to 10^{-1} Hz lower frequency region. The values of imaginary parts almost remain unchanged within a frequency range of 10^6–10^5 Hz, the values gradually increased at 10^5–10^3 Hz and decreased at 10^3–10^1 Hz; and these values then slowly increased in the 10^1 to 10^{-1} Hz lower frequency region. Roberts and Tyburczy (1991) and Saltas et al. (2013) have suggested that the ideal semicircle represents the bulk electrical properties of a sample, and the additional tail is characteristic of diffusion processes at the sample–electrode interface. Hence, the bulk sample resistance can be obtained by fitting the ideal semicircle in the high frequency domain. A series connection of resistance and constant phase elements (R_S–CPE_S) and the interaction of charge carriers with the electrode (R_E–CPE_E) was applied to be the equivalent circuit. All fitting errors of the electrical resistance were less than 5%. Based on the sample size and electrical resistance, the electrical conductivity of the sample was calculated:

$$\sigma = L / SR \quad (1)$$

where L is the height of the sample (m), S is the cross-sectional area of the electrodes (m^2), R is the fitting resistance (Ω) and σ is the electrical conductivity of the sample (S/m).

The logarithmic electrical conductivities of the gneiss samples were plotted against the reciprocal temperatures under conditions of 623–1073 K and 0.5–2.0 GPa. The electrical conductivities of gneiss with X_A=7.12% were measured in two sequential heating and cooling cycles at 1.5 GPa (Fig. 5). After the first heating cycle, electrical conductivities of the gneiss at the same temperature were close to each other in other cycles. We confirmed that our experimental data were reproducible, and the gneiss sample was kept at a steady state after the first heating cycle. Two different linear relationships of logarithmic electrical conductivity and reciprocal temperature were separated by an inflection point. The electrical conductivity of gneiss with W_A=7.12% significantly increased with temperatures above 723 K at 0.5–1.0 GPa, and this phenomenon occurred after 773 K at 1.5–2.5 GPa (Fig. 6). The electrical conductivity of the samples increased with pressure, but the effect of pressure on conductivity was

weaker than temperature. For other gneiss samples (W_A=7.27% and 7.64%), the inflection points appeared at 773 K under all designated pressures (Fig. 7). In a specific temperature range, the relationship between electrical conductivity and temperature fits the Arrhenius formula:

$$\sigma = \sigma_0 \exp(-\Delta H / kT) \quad (2)$$

$$\Delta H = \Delta U + P\Delta V \quad (3)$$

where σ_0 is the pre-exponential factor (S/m), ΔH is the activation enthalpy (eV), k is the Boltzmann constant (eV/K), T is the absolute temperature (K), ΔU is the activation energy (eV), P is the pressure (GPa) and ΔV is the activation volume (cm^3/mole). All fitting parameters for the electrical conductivities of three gneiss samples are listed in Table 3. The activation enthalpy values (ΔH) for the gneiss samples are 0.35–0.58 eV in the lower temperature region and 0.71–1.05 eV in the higher temperature region, respectively. In addition, the logarithms of pre-exponential factor values (Log σ_0) were transformed from negative to positive from the correspondent lower to the higher temperature ranges.

The total alkali and calcium ion content of K_2O, Na_2O and CaO is a remarkable influence on the electrical conductivities of the gneiss samples. As shown in Figure 7, the electrical conductivity of the gneiss samples increased with the total weight percent of K_2O, Na_2O and CaO. It reflects the fact the electrical conductivity of the gneiss samples is controlled mainly by minerals that contain abundant K_2O, Na_2O and CaO. The cations of feldspar are K^+, Na^+ and Ca^{2+}, and K^+ is also the main cation of biotite. Furthermore, impurity ions (K^+, Na^+ and Al^{3+}) have been suggested to be the charge carriers for quartz samples (Wang et al., 2010). In addition, the electrical conductivity of the gneiss samples do not regularly change with variations in biotite-bearing content (Fig. 7 and Table 1). Based on all of the experimental results, the biotite content is not the main influential factor on the electrical conductivity of gneiss. Therefore, we cannot distinguish the specific mineral that controls the electrical conductivity of the gneiss samples. However, it was reasonable to consider the gneiss sample as a complex whole,

and analyze the electrical conductivity of gneiss with various chemical compositions at high temperature and pressure.

4 Discussions

4.1 A comparison with previous studies

As three constituent minerals of gneiss, feldspar, biotite and quartz dominated the electrical conductivity of the whole rock at high temperature and pressure. Due to their sophisticated mineralogical assemblage and rock structure, the gneiss samples were unstable in the first heating cycle. In this process, the impurity ions may have been distributed, the grain size slightly changed and the microfractures gradually closed. After the first cycle, the electrical conductivity of the gneiss samples had good repeatability. This suggested that the gneiss samples were in a stable state. The electrical conductivity range of the gneiss samples with various chemical compositions was about 10^{-5}–10^{-1} S/m at 623–973 K and 0.5–2.0 GPa. The electrical conductivity was slightly related to pressure, and conforms to previous conclusions that the influence of pressure on mineral and rock conductivity is much weaker than temperature (Xu et al., 2000; Hu et al., 2011; Dai and Karato, 2014a, b). The possible reason is that the effect of pressure on the activity of the charge carriers is weaker than temperature. The total alkaline ion content of K_2O, Na_2O and CaO has crucial influence on the electrical conductivity of gneiss. Previous studies have investigated the electrical conductivity of minerals and rocks with various chemical compositions, and the conclusions were similar to ours (Dai et al., 2014). Fiji-ta et al. (2007) performed the electrical conductivity of gneiss perpendicular and parallel to foliation at up to 1000 K and a constant pressure of 1.0 GPa. The conductivity of gneiss measured perpendicular to foliation was one order of magnitude lower than the value measured parallel to foliation. However, the influence of pressure and chemical composition on the electrical conductivity of gneiss has not been studied. In the present work, we investigated the electrical conductivity of gneiss parallel to foliation. As shown in Figure 8, the electrical conductivity of gneiss from

Fuji-ta et al. (2007) was higher than our results in the lower temperature range, and values were lower than the conductivity of gneiss with W_A= 7.27% and 7.64% in this study. This discrepancy is probably caused by varying chemical compositions of the gneiss samples. Dai et al. (2014) measured the electrical conductivity of granite at 0.5–1.5 GPa and 623–1173 K, and the main rock-forming minerals were also quartz, feldspar, and biotite. They found that the content of calcium and alkali ions significantly affected the electrical conductivity of granite under conditions of high temperature and high pressure. Electrical conductivities of granite and gneiss increased with calcium and alkali ion content. However, the electrical conductivity of granite was much lower than gneiss (Fig. 8). This difference may be caused by the various chemical compositions and rock structures between granite and gneiss. Feldspars are main constituent rock-forming minerals in gneiss, and thus it is important to compare the electrical conductivity of feldspar. The electrical conductivity of K-feldspar is one order of magnitude lower than albite, and K^+ and Na^+ ions are the charge carriers of K-feldspar and albite, respectively (Hu et al., 2013). As shown in Figure 8, the electrical conductivity of alkali feldspar is much higher than the gneiss samples. This may be because the concentration of alkali ions in feldspar is higher than gneiss. In addition, granulite is another significant metamorphic rock, and usually coexists with gneiss. The electrical conductivity of granulite is moderately higher than gneiss. The electrical conductivity of quartz at 1.0 GPa is slightly lower than gneiss with X_A=7.27% at 1.5 GPa, and the slope of the linear relationship between the logarithm of electrical conductivity and the reciprocal of temperature for quartz is close to gneiss in a lower temperature range (Wang et al., 2010). The conductivity of phlogopite is higher than gneiss with X_A=7.64% at higher temperatures (>773 K), and lower than gneiss samples at lower temperatures (<773 K). Furthermore, the slope of the linear relationship between the logarithm of electrical conductivity for the phlogopite and the reciprocal temperature is much higher than the slope of the gneiss samples (Li et al., 2016). Compared with Ferri et al. (2013), the electrical conductivity of the garnet–biotite–sillimanite residual enclave (JOY2-X4) was very close to our conductivity results for the run DS13 and DS14 gneiss samples in the lower temperature and higher temperature

regions, respectively. The electrical conductivity of sample JOY2-X4 was slightly lower than the run DS12gneiss sample. In addition, the electrical conductivity of natural metapelite (PP216) from Hashim et al. (2013) was close to the values of the run DS12 gneiss sample in the lower temperature region, and the slope between logarithmic conductivities and reciprocal temperature for the PP216 metapelite was higher than the gneiss samples in the higher temperature region.

4.2 Conduction mechanism

The logarithm of electrical conductivities and reciprocal temperatures showed linear relationships at the lower and higher temperature ranges, respectively. This implies that the dominant conduction mechanism for our gneiss samples in the lower temperature range is different from the higher temperature range. The mineral assemblage and chemical composition of gneiss samples are very complicated, and thus the conduction mechanisms for gneiss samples are difficult to determine. Feldspar, quartz and biotite are the dominant minerals in the gneiss samples. Previous studies have suggested that the conduction mechanism for feldspar minerals is ionic conduction and the charge carriers are K^+, Na^+ and Ca^{2+} (Hu et al., 2013). The conduction mechanism for biotite has not been studied, whereas the charge carriers of phlogopite were proposed to be F^- and K^+ (Li et al., 2016). For quartz, the conduction mechanism was impurity ionic conduction, and the dominant charge carriers migrate by moving the alkali ions in channels (Wang et al., 2010). Therefore, we deduced that the conduction mechanism for gneiss samples may be related to ions. The activation enthalpy is one crucial evidence for the conduction mechanism of minerals and rocks (Dai et al., 2016). The activation enthalpies for gneiss samples are 0.35–0.58 eV in the lower temperature region, and 0.77–0.87 eV in the higher temperature region (Table 3). Dai et al. (2014) studied the electrical conductivity of granite that had the same mineralogical assemblage as the gneiss samples. They proposed that the conduction mechanism at the lower temperature range was the impurity conduction owing to the low activation enthalpy (0.5 eV), whereas the mechanism was ionic conduction with a high activation

enthalpy (1.0 eV) at the higher temperature range. The activation enthalpy for gneiss was close to the values for granite at the lower and higher temperature ranges. The activation enthalpies for albite and K-feldspar were 0.84 and 0.99 eV, respectively (Hu et al., 2013). With increasing pressure, the electrical conductivity of gneiss increased accordingly. The activation volumes for one gneiss sample (DS12) were -7.10 cm^3/mole and -2.69 cm^3/mole in the low and high temperature regions, respectively. We can compare gneiss with the electrical conductivity of eclogite, another representative metamorphic rock. Recently, Dai et al. (2016) measured the electrical conductivity of dry eclogite and the negative activation volume for eclogite was -2.51 cm^3/mole under 1.0–3.0 GPa and 873–1173 K. It was proposed that the main conduction mechanism for dry eclogite is intrinsic conduction (Dai et al., 2016). In addition, Figure 7 shows that the increasing content of alkali and calcium ions significantly enhances the electrical conductivity of gneiss samples. Therefore, the impurity conduction (possible charge carriers: K^+, Na^+, Ca^{2+} and H^+) and ionic conduction (possible charge carriers: K^+, Na^+ and Ca^{2+}) are suggested to be the conduction mechanisms at lower and higher temperature ranges, respectively.

4.3 Effect of chemical composition on electrical conductivity

The influence of chemical composition (Na_2O+K_2O+CaO) on the electrical conductivity of the gneiss samples was very significant, as shown in a previous study that the electrical conductivity of granite samples is closely related to the alkali and calcium ion content (Dai et al., 2014). The electrical conductivity of granite samples at high temperature and pressure can be fitted as a function of (Na_2O+K_2O+CaO)/SiO_2 (Dai et al., 2014). However, the electrical conductivity of gneiss samples does not regularly change with variations in (Na_2O+K_2O+CaO)/SiO_2. This may be due to the more complicated mineralogical assemblage and chemical composition of gneiss: for mineralogical assemblage, the biotite content of the gneiss sample is higher than granite; as for the chemical compositions, the contents of SiO_2 for gneiss are lower than those of granite samples; the contents of the calc-alkali ions are approximate between gneiss

and granite samples. Hu et al. (2013) demonstrated that the electrical conductivity of alkali feldspar significantly depends on the value of Na/(Na+K). This suggests that the electrical conductivity of gneiss is affected by the total content of alkali and calcium ions, as well as the ratios between various ions.

5 Geophysical implications

As a typical metamorphic rock in the present research region, gneiss is widespread in the UHPM zone (Zheng et al., 2003; Liu et al., 2005; Hashim et al., 2013). The geological map of the Dabie–Sulu orogenic belt and its corresponding lithological distribution in the southern Dabie–Sulu region are displayed in Figure 9. As one of the largest UHPM belts in the world for Dabie–Sulu orogen, gneiss is the outcropping rock directly in contact with eclogite, and occupies up to 90% of the exposed metamorphic rock area. Therefore, the in situ laboratory-based electrical conductivity of gneiss at high temperature and pressure is very significant to interpret the conductivity structure in the Dabie–Sulu belt, deep in the Earth's interior. The Dabie terrane is a major segment bounded by the Tan–Lu fault to the east and separated into a series of continuous zones by several large-scale E–W trending faults; the Sulu terrane is segmented into a number of blocks by several NE–SW trending faults subparallel to the Tan–Lu fault (Zheng, 2008; Xu et al., 2013). The discovery of coesite and/or diamond inclusions in various types of rock (e.g., gneiss, eclogite, amphibolite, marble and jadeite quartzite) through the Dabie–Sulu orogen indicates that continental crust has been subducted at a depth of 80–200 km and subsequently exhumed to the Earth's surface. During subduction, dehydration reactions of some hydrous minerals (e.g., lawsonite, phengite and chlorite) and partial melting of other regional metamorphic rocks (e.g., gneiss and eclogite) occur at high temperature and pressure (Xu et al., 2013; Liu et al., 2014). Previous field MT results have found that high conductivity anomalies with magnitudes of 10^{-1} S/m are widely distributed at 10–20 km in the Dabie–Sulu UHPM belt (Xiao et al., 2007). In addition, the slab-like high velocity anomaly results have also confirmed a depth of ≥110 km for the uppermost mantle beneath the Dabie–

Sulu orogen, which represents a remnant of the subducted Yangtze block after Triassic continent–continent collision (Xu et al., 2001). However, the origin and causal mechanisms of these high conductivity anomalies for the Dabie–Sulu UHPM belt are still unknown. Together with the two main constituent rocks (natural eclogite and granulite) in the UHPM belt, it is crucial to explore whether the gneiss electrical conductivity can be used to interpret the high conductivity anomalies distributed in the Dabie–Sulu tectonic belt. The relationship between temperature and depth in the Earth's stationary crust can be obtained by a numerical solution of the heat conduction equation (Selway et al., 2014):

$$T = T_0 + (\frac{Q}{k})Z - (\frac{A_0}{2k})Z^2 \quad (4)$$

where T_0 is the surface temperature (K), Q is the surface heat flow (mW/m^2), Z is the lithosphere layer depth (km), k is thermal conductivity (W/mK), and A_0 is the lithospheric radiogenic heat productivity (μW/m^3). Based on previous studies, the corresponding thermal calculation parameters for the Dabie–Sulu orogen are Q=75 mW/m^2 (He et al., 2009), A_0=0.31 μW/m^3 and k=2.6 W/mK (Zhou et al., 2011).

Based on the heat conduction equation (Eq. 4) and thermal calculation parameters, the conductivity–temperature results of gneiss with various chemical compositions (W_A=Na_2O+K_2O+CaO=7.12%, 7.27% and 7.64%) can be converted to a conductivity–depth profile for the Dabie–Sulu orogen (Fig. 10). A similar transformation was also conducted for granulite by Fuji-ta et al. (2004) and eclogite with different oxygen fugacity (Cu+CuO, Ni+NiO, and Mo+MoO_2) by Dai et al. (2016). Figure 10 makes clear that the high conductivity anomaly of $10^{-1.5}$–$10^{-0.5}$ S/m from the field MT results in the Dabie–Sulu UHPM belt occurs at 12–21 km, compared with three dominant constituent rock conductivities of gneiss, granulite and eclogite in the region. Although our obtained electrical conductivity of gneiss with different chemical compositions is moderately higher than granulite and eclogite, it is not high enough to explain the high conductivity anomaly observed in field MT results in the Dabie–Sulu orogen. In other words, three dominant outcrops of metamorphic rocks, including gneiss, eclogite and granulite, are not substances that produce the high conductivity anomalies of the Dabie–

389 Sulu orogen. However, the conductivity–depth profile for gneiss with various chemical
390 compositions may provide an important constraint on the interpretation of field
391 magnetotelluric conductivity results in the regional UHPM belt.
392 Aside from the chemical composition, other available alternative causes for high
393 conductivity anomalies can be considered, such as water in nominally anhydrous
394 minerals (Wang et al., 2006; Yang, 2011; Dai and Karato, 2009, 2014a), interconnected
395 saline (or aqueous) fluids (Hashim et al., 2013; Shimojuku et al., 2014; Sinmyo and
396 Keppler, 2017; Guo et al., et al., 2015; Li et al., 2018), partial melting (Wei et al., 2001;
397 Maumus et al., 2005; Gaillard et al., 2008; Ferri et al., 2013; Laumonier et al., 2015,
398 2017; Ghosh and Karki, 2017), interconnected secondary high-conductivity phases (e.g.,
399 FeS, Fe_3O_4) (Jones et al., 2005; Bagdassarov et al., 2009; Padilha et al., 2015),
400 dehydration of hydrous minerals (Wang et al., 2012, 2017; Manthilake et al., 2015, 2016;
401 Hu et al., 2017; Sun et al., 2017a, b; Chen et al., 2018) and graphite films on mineral
402 grain boundaries (Freund, 2003; Pous et al., 2004; Chen et al., 2017). In consideration
403 of the similar formation conduction and geotectonic environments, the Himalaya–
404 Tibetan orogenic system was compared with the Dabie–Sulu UHPM belt, and explained
405 high electrical conductivity anomalies. Previous evidences from magnetotelluric and
406 elastic seismic velocity data in the southern Tibet and northwestern Himalaya zones
407 have confirmed that the high conductivity and low seismic velocity anomalies
408 widespread exist at 10–25 km in the Himalaya–Tibetan orogenic system (Wei et al.,
409 2001; Unsworth et al., 2005; Arora et al., 2007; Caldwell et al., 2009). Some studies
410 have hypothesized that partial melting is the cause of the high conductivity anomalies
411 in the Himalaya–Tibetan orogenic system (Wei et al., 2001; Gaillard et al., 2004;
412 Hashim et al., 2013). Nevertheless other researchers think they are closely related with
413 interconnected aqueous fluid (Makovsky and Klempere, 1999). As argued by Li et al.
414 (2003), five possible hypotheses could explain the cause for the high conductivity
415 anomalies in the INDEPTH magnetotelluric data of the southern Tibet mid-crust. The
416 authors found that the high conductivity anomalies may be a result of interconnected
417 melt and fluids. Recently, Naif et al. (2018) suggested that the high conductivity
418 anomaly at 50–150 km can be explained by either a small amount of water stored in

nominally anhydrous minerals or interconnected partial melts. In the present study, the electrical conductivity of gneiss with various chemical compositions at high temperature and pressure cannot be used to interpret the high conductivity anomalies of the Dabie–Sulu UHPM belt. Therefore, we propose that it is possibly caused by interconnected fluids or melts that result in high conductivity anomalies for the Dabie–Sulu UHPM belt.

6 Conclusions

The electrical conductivity range of gneiss samples with various chemical compositions was about 10^{-5}–10^{-1} S/m at 623–1073 K and 0.5–2.0 GPa. Electrical conductivity of the gneiss samples significantly increased with temperature, and weakly increased with pressure. The total alkaline ion content of K_2O, Na_2O and CaO is a remarkable influence on the electrical conductivity of the gneiss samples. Based on various activation enthalpy ranges (0.35–0.52 eV and 0.76–0.87 eV), corresponding to higher and lower temperature regions at 1.5 GPa, two main conduction mechanisms are suggested to dominate the conductivity of gneiss: impurity conduction in the lower temperature region and ionic conduction (charge carriers are K^+, Na^+ and Ca^{2+}) in the higher temperature region. Because of the much lower conductivity of gneiss samples at high temperature and pressure, we confirmed that gneiss with various chemical compositions cannot cause the high conductivity anomalies in the Dabie–Sulu UHPM belt.

Acknowledgements. We thank the editor of Professor Ulrike Werban and three anonymous reviewers for their very constructive comments and suggestions in the reviewing process, which helped us greatly in improving the manuscript. We appreciate Dr Kara Bogus from Edanz Group (www.edanzediting.com/ac) Scientific Editing Company for their helps in English improvements of the manuscript. This research was financially supported by the Strategic Priority Research Program (B) of the Chinese Academy of Sciences (XDB 18010401), Key Research Program of Frontier Sciences of CAS (QYZDB-SSW-DQC009), "135" Program of the Institute of Geochemistry of CAS, Hundred Talents Program of CAS and NSF of China (41474078, 41774099 and 41772042).

References

Arora, B.R., Unsworth, M.J., and Rawat, G.: Deep resistivity structure of the northwest Indian Himalaya and its tectonic implications. Geophys. Res. Lett., 34, L04307, 2007, doi: http://dx.doi.org/10.1029/2006GL029165.

Bagdassarov, N., Golabek, G.J., Solferion, G., and Schmidt, M.W.: Constraints on the Fe-S melt connectivity in mantle silicates from electrical impedance measurements. Phys. Earth Planet. Inter., 177, 139–146, 2009.

Caldwell, W.B., Klemperer, S.L., Rai, S.S., and Lawrence, J.F.: Partial melt in the upper-middle crust of northwest Himalaya are veiled by Rayleigh wave dispersion. Tectonophysics, 477, 58–65, 2009.

Chen, J.Y., Yang, X.S., and Chen, J.Y.: Experimental studies on the relationship between carbonaceous structure and electrical conductivity of the Longmenshan fault zone. Chinese J. Geophys., 60, 3475–3492, 2017.

Chen, S.B., Guo, X.Z., Yoshino, T., Jin, Z.M., and Li, P.: Dehydration of phengite inferred by electrical conductivity measurements: Implication for the high conductivity anomalies relevant to the subduction zones. Geology, 46, 11–14, 2018.

Dai, L.D., and Karato, S.I.: High and highly anisotropic electrical conductivity of the asthenosphere due to hydrogen diffusion in olivine. Earth Planet. Sci. Lett., 408, 79–86, 2014a.

Dai, L.D. and Karato, S.: Influence of FeO and H on the electrical conductivity of olivine. Phys. Earth Planet. Inter., 237, 73–79, 2014b.

Dai, L.D., and Karato, S.I.: Electrical conductivity of wadsleyite at high temperatures and high pressures. Earth Planet. Sci. Lett., 287, 277–283, 2009.

Dai, L.D., Hu, H.Y., Li, H.P., Wu, L., Hui, K.S., Jiang, J.J., and Sun, W.Q.: Influence of temperature, pressure, and oxygen fugacity on the electrical conductivity of dry eclogite, and geophysical implications. Geochem. Geophys. Geosyst., 17, 2394–2407, 2016.

Dai, L.D., Hu, H.Y., Li, H.P., Jiang, J.J., and Hui, K.S.: Influence of temperature, pressure, and chemical composition on the electrical conductivity of granite. Am.

Mineral., 99, 1420–1428, 2014.

Dai, L.D., Li, H.P., Hu, H.Y., Shan, S.M., Jiang, J.J., and Hui, K.S.: The effect of chemical composition and oxygen fugacity on the electrical conductivity of dry and hydrous garnet at high temperatures and pressures. Contrib. Mineral. Petrol., 163, 689–700, 2012.

Dai, L.D., Li, H.P., Hu, H.Y., and Shan S.M.: Experimental study of grain boundary electrical conductivities of dry synthetic peridotite under high-temperature, high-pressure, and different oxygen fugacity conditions. J. Geophys. Res., 113, B12211, 2008, doi: 10.1029/2008JB005820.

Ferri, F., Gibert, B., Violay, M., and Cesare, B. Electrical conductivity in a partially molten crust from measurements on metasedimentary enclaves. Tectonophysics, 586, 84–94, 2013.

Freund, F.: On the electrical conductivity structure of the stable continental crust. J. Geodyn., 35, 353–388, 2003.

Fuji-ta, K., Katsura, T., Matsuzaki, T., Ichiki, M., and Kobayashi, T.: Electrical conductivity measurement of gneiss under mid- to lower crustal *P-T* conditions. Tectonophysics, 434, 93–101, 2007.

Fuji-ta, K., Katsura, T., and Tainosho, Y.: Electrical conductivity measurement of granulite under mid- to lower crustal pressure-temperature conditions. Geophys. J. Int., 157, 79–86, 2004.

Gaillard, F., Malki, M., Iacono-Marziano, G., Pichavant, M., and Scaillet, B.: Carbonatite melts and electrical conductivity in the asthenosphere. Science, 322, 1363–1365, 2008.

Gaillard, F., Scaillet, B., and Pichavant, M.: Evidence for present-day leucogranite pluton growth in Tibet. Geology, 32, 801–804, 2004.

Ghosh, D.B., and Karki, B.B.: Transport properties of carbonated silicate melt at high pressure. Sci. Adv., 3, e1701840, 2017, doi: 10.1126/sciadv.1701840.

Guo, X.Z., Yoshino, T., and Shimojuku, A.: Electrical conductivity of albite–(quartz)–water and albite–water–NaCl systems and its implication to the high conductivity anomalies in the continental crust. Earth Planet. Sci. Lett., 412, 1–9, 2015.

539 Hashim, L., Gaillard, F., Champallier, R., Breton, N. L., Arbaret, L., and Scaillet, B.:
540 Experimental assessment of the relationships between electrical resistivity, crustal
541 melting and strain localization beneath the Himalayan-Tibetan Belt. Earth Planet.
542 Sci. Lett., 373, 20–30, 2013.
543 He, L., Hu, S., Yang, W., and Wang, J.: Radiogenic heat production in the lithosphere
544 of Sulu ultrahigh-pressure metamorphic belt. Earth Planet. Sci. Lett., 277, 525–
545 538, 2009.
546 Hu, H.Y., Dai, L.D., Li, H.P., Hui, K.S., and Sun, W.Q.: Influence of dehydration on
547 the electrical conductivity of epidote and implications for high conductivity
548 anomalies in subduction zones. J. Geophys. Res., 122, 2751–2762, 2017.
549 Hu, H.Y., Li, H.P., Dai, L.D., Shan, S.M., and Zhu, C.M.: Electrical conductivity of
550 alkali feldspar solid solutions at high temperatures and high pressures. Phys. Chem.
551 Miner., 40, 51–62, 2013.
552 Hu, H.Y., Li, H.P., Dai, L.D., Shan, S.M., and Zhu, C.M.: Electrical conductivity of
553 albite at high temperatures and high pressures. Am. Mineral., 96, 1821–1827, 2011.
554 Hui, K.S., Zhang, H., Li, H.P., Dai, L.D., Hu, H.Y., Jiang, J.J., and Sun, W.Q.:
555 Experimental study on the electrical conductivity of quartz andesite at high
556 temperature and high pressure: Evidence of grain boundary transport. Solid Earth,
557 6, 1037–1043, 2015.
558 Jones, A.G., Ledo, J., and Ferguson, I.J.: Electromagnetic images of the Trans-Hudson
559 Orogen: The North American Central Plains anomaly revealed. Can. J. Earth Sci.,
560 42, 457–478, 2005.
561 Laumonier, M., Gaillard, F., Muir, D., Blundy, J., and Unsworth, M.: Giant magmatic
562 water reservoirs at mid-crustal depth inferred from electrical conductivity and the
563 growth of the continental crust. Earth Planet. Sci. Lett., 457, 173–180, 2017.
564 Laumonier, M., Gaillard, F., and Sifre, D.: The effect of pressure and water
565 concentration on the electrical conductivity of dacitic melts: Implication for
566 magnetotelluric imaging in subduction areas. Chem. Geol., 418, 66–76, 2015.
567 Li, P., Guo, X.Z., Chen, S.B., Wang, C., Yang, J.L., and Zhou, X.F.: Electrical
568 conductivity of the plagioclase–NaCl–water system and its implication for the

high conductivity anomalies in the mid-lower crust of Tibet Plateau. Contrib. Mineral. Petrol., 173, 16, 2018, doi: https://doi.org/10.1007/s00410-018-1442-9.

Li, S., Unsworth, M., Booker, J., Wei, W., Tan, H., and Jones, A.G.: Partial melt or aqueous fluid in the mid-crust of Southern Tibet? Constraints from INDEPTH magnetotelluric data. Geophys. J. Int., 153, 289–304, 2003.

Li, Y., Yang, X.Z., Yu, J.H., and Cai, Y.F.: Unusually high electrical conductivity of phlogopite: The possible role of fluorine and geophysical implications. Contrib. Mineral. Petrol., 171, 37, 2016, doi: 10.1007/s00410-016-1252-x.

Liu, P., Wu, Y., Liu, Q., Zhang, J.F., Zhang, L., and Jin, Z.M.: Partial melting of UHP calc-gneiss from the Dabie Mountains. Lithos, 192–195, 86–101, 2014.

Liu, F.L., Xu, Z.Q., Yang, J.S., Zhang, Z.M., Xue, H.M., Meng, F.C., Li, T.F. and Cheng, S.Z.: Geochemical characteristics and genetic mechanism of orthgneiss and paragneiss in the depth intervals of 2000–3000 m from main drill hole of Chinese Continental Scientific Drilling Project. Acta Petrol. Sin., 21, 305–324, 2005.

Makovsky, Y. and Klemperer, S.L.: Measuring the seismic properties of Tibetan bright spots: Evidence for free aqueous fluids in the Tibetan middle crust. J. Geophys. Res., 104, 10795–10825, 1999.

Manthilake, G., Bolfan-Casanova, N., Novella, D., Mookherjee, M., and Andrault, D.: Dehydration of chlorite explains anomalously high electrical conductivity in the mantle wedges. Sci. Adv., 2, e1501631, 2016, doi: 10.1126/sciadv.1501631.

Manthilake, G., Mookherjee, M., Bolfan-Casanova, N., and Andrault, D.: Electrical conductivity of lawsonite and dehydrating fluids at high pressures and temperatures. Geophys. Res. Lett., 42, 7398–7405, 2015.

Maumus, J., Bagdassarov, N., and Schmeling, H.: Electrical conductivity and partial melting of mafic rocks under pressure. Geochim. Cosmochim. Ac., 69, 4703–4718, 2005.

Naif, S.: An upper bound on the electrical conductivity of hydrated oceanic mantle at the onset of dehydration melting. Earth Planet. Sci. Lett., 482, 357–366, 2018.

Novella, D., Jacobsen, B., Weber, P.K., Tyburczy, J.A., Ryerson, F.J., and Du Frane, W.L.: Hydrogen self-diffusion in single crystal olivine and electrical conductivity

599 of the earth's mantle. Sci. Rep., 7, 5344, 2017, doi: 10.1038/s41598-017-05113-6.
600 Padilha, A.L., Vitorello, I., Antunes, C.E., and Padua, M.B.: Imaging three-dimensional
601 crustal conductivity structures reflecting continental flood basalt effects hidden
602 beneath thick intracratonic sedimentary basin. J. Geophys. Res., 120, 4702–4719,
603 2015.
604 Pape, L.P., Jones, A.G., Unsworth, M.J., Vozar, J., Wei, W.B., Jin, S., Ye, G.F., Jing,
605 J.N., Dong, H., Zhang, L.T., and Xie, C.L.: Constraints on the evolution of crustal
606 flow beneath Northern Tibet. Geochem. Geophys. Geosyst., 12, 4237–4260, 2015.
607 Pous, J., Munoz, G., Heise, W., Melgarejo, J.C., and Quesada, C.: Electromagnetic
608 imaging of Variscan crustal structures in SW Iberia: The role of interconnected
609 graphite. Earth Planet. Sci. Lett., 217, 435–450, 2004.
610 Roberts, J.J. and Tyburczy, J.A.: Frequency dependent electrical properties of
611 polycrystalline olivine compacts. J. Geophys. Res., 96, 16205–16222, 1991.
612 Saltas, V., Chatzistamou, V., Pentari, D., Paris, E., Triantis, D., Fitilis, I., and
613 Vallianatos, F.: Complex electrical conductivity measurements of a KTB
614 amphibolite sample at elevated temperatures. Mater. Chem. Phys., 139, 169–175,
615 2013.
616 Selway, K., Yi, J., and Karato, S.: Water content of the Tanzanian lithosphere from
617 magnetotelluric data: Implications for cratonic growth and stability. Earth Planet.
618 Sci. Lett., 388, 175–186, 2014.
619 Shimojuku, A., Yoshino, T., and Yamazaki, D.: Electrical conductivity of brine-bearing
620 quartzite at 1 GPa: Implications for fluid content and salinity of the crust. Earth
621 Planets Space, 66, 1–9, 2014.
622 Sinmyo, R. and Keppler, H.: Electrical conductivity of NaCl-bearing aqueous fluids to
623 600 °C and 1 GPa. Contrib. Mineral. Petrol., 172, 4, 2017, doi: 10.1007/s00410-
624 016-1323-z.
625 Sun, W.Q., Dai, L.D., Li, H.P., Hu, H.Y., Wu, L., and Jiang, J.J.: Electrical conductivity
626 of mudstone before and after dehydration at high temperatures and pressures. Am.
627 Mineral., 102, 2450–2456, 2017a.
628 Sun, W.Q., Dai, L.D., Li, H.P., Hu, H.Y., Jiang, J.J., and Hui, K.S.: Effect of dehydration

on the electrical conductivity of phyllite at high temperatures and pressures. Mineral. Petrol., 111, 853–863, 2017b.

Unsworth, M.J., Jones, A.G., Wei, W., Marquis, G., Gokarn, S.G., and Spratt, J.E. Project ININDEPTH Team: Crustal rheology of the Himalaya and southern Tibet inferred from magnetotelluric data. Nature, 438, 78–81, 2005.

Wang, D.J, Liu, X.W., Liu, T., Shen, K.W., Welch, D.O., and Li, B.S.: Constraints from the dehydration of antigorite on high-conductivity anomalies in subduction zones. Sci. Rep., 7, 16893, 2017, doi: 10.1038/s41598-017-16883-4.

Wang, D.J., Guo, X.Y., Yu, Y.J., and Karato, S.: Electrical conductivity of amphibole-bearing rocks: Influence of dehydration. Contrib. Mineral. Petrol., 164, 17–25, 2012.

Wang, D.J., Li, H.P., Matsuzaki, T., and Yoshino, T.: Anisotropy of synthetic quartz electrical conductivity at high pressure and temperature. J. Geophys. Res., 115, B09211, 2010, doi: 10.1029/2009JB006695.

Wang, D.J., Mookherjee, M., Xu, Y.S., and Karato, S.: The effect of water on the electrical conductivity of olivine. Nature, 443, 977–980, 2006.

Wannamaker, P.E., Caldwell, T.G., Jiracek, G.R., Maris, V., Hill, G.J., Ogawa, Y., Bibby, H.M., Bennie, S.L., and Heise, W.: Fluid and deformation regime of an advancing subduction system at Marlborough, New Zealand. Nature, 460, 733–736, 2009.

Wei, W., Unsworth, M., Jones, A.G., Booker, J., Tan, H., Nelson, K.D., Chen, L., Li, S., Solon, K., and Bedrosian, P.: Detection of wide spread fluids in the Tibetan crust by magnetotelluric studies. Science, 292, 716–718, 2001.

Xiao, Q.B., Cai, X.P., Liang, G.H., Xu, X.W., and Zhang, B.L.: Application of 2D magnetotelluric methods in a geological complex area, Xinjiang, China. J. Appl. Geophys., 75, 19–30, 2011.

Xiao, Q.B., Zhao, G.Z., Zhan, Y., Chen, X.B., Tang, J., Wang, J.J., and Deng, Q.H.: A preliminary study on electrical structure and dynamics of the ultra-high pressure metamorphic belt beneath the Dabie Mountains. Chinese J. Geophys., 50, 710–721, 2007.

Xu, P.F., Liu, F.T., Wang, Q.C., Cong, B.L., and Chen, H.: Slab-like high velocity

anomaly in the uppermost mantle beneath the Dabie-Sulu orogen. Geophys. Res. Lett., 28, 1847–1850, 2001.

Xu, H.J., Ye, K., Song, Y.R., Chen, Y., Zhang, J.F., Liu, Q., and Guo, S.: Prograde metamorphism, decompressional partial melting and subsequent melt fractional crystallization in the Weihai migmatitic gneisses, Sulu UHP terrane, eastern China. Chem. Geol., 341, 16–37, 2013.

Xu, Y.S., Shankland, T.J., and Duba, A.G.: Pressure effect on electrical conductivity of mantle olivine. Phys. Earth Planet. Inter., 118, 149–161, 2000.

Yang, X.Z., Keppler, H., McCammon, C., and Ni, H.W.: Electrical conductivity of orthopyroxene and plagioclase in the lower crust. Contrib. Mineral. Petrol., 163, 33–48, 2012.

Yang, X.Z.: Origin of high electrical conductivity in the lower continental crust: A review. Surv. Geophys., 32, 875–903, 2011.

Zeng, S.H., Hu, X.Y., Li, J.H., Xu, S., Fang, H., and Cai, J.C.: Detection of the deep crustal structure of the Qiangtang terrane using magnetotelluric imaging. Tectonophysics, 661, 180–189, 2015.

Zheng, Y.F.: A perspective view on ultrahigh-pressure metamorphism and continental collision in the Dabie-Sulu orogenic belt. Chinese Sci. Bull., 53, 3081–3104, 2008.

Zheng, Y.F., Fu, B., Gong, B., and Li, L.: Stable isotope geochemistry of ultrahigh pressure metamorphic rocks from the Dabie-Sulu orogen in China: Implications for geodynamics and fluid regime. Earth-Sci. Rev., 62, 105–161, 2003.

Zhou, W.G., Fan, D.W., Liu, Y.G., and Xie, H.S.: Measurements of wave velocity and electrical conductivity of an amphibolite from southwestern margin of the Tarim Basin at pressures to 1.0 GPa and temperatures to 700 °C: Comparison with field observations. Geophys. J. Int., 187, 1393–1404, 2011.

689 **Figure captions**

690 **Fig. 1** Photomicrographs and electron backscattered images of three natural gneiss
691 samples under the polarizing microscope. Pl=plagioclase; Qtz = quartz and
692 Bt = biotite.

693 **Fig. 2** Experimental setup for electrical conductivity measurements at high
694 temperatures and pressures.

695 **Fig. 3** Representative complex impedance spectra for run DS12 gneiss under conditions
696 of 1.5 GPa and 623–1073 K.

697 **Fig 4.** Real and imaginary parts of complex impedance as functions of the measured
698 frequencies for the runs DS13 and DS14 gneiss samples under conditions of 1.5
699 GPa and 623–1073 K. (a) real and (b) imaginary parts for the run DS13 gneiss; (c)
700 real and (d) imaginary parts for the run DS14 gneiss.

701 **Fig. 5** Logarithm of the electrical conductivities versus the reciprocal temperatures for
702 run DS12 gneiss during two heating/cooling cycles at 1.5 GPa.

703 **Fig. 6** Logarithm of the electrical conductivities versus the reciprocal temperatures for
704 run DS12 gneiss at 0.5–2.5 GPa and 623–1073 K.

705 **Fig. 7** Logarithm of the electrical conductivities versus the reciprocal temperatures of
706 the gneiss samples with various chemical compositions at 1.5 GPa and 623–
707 1073 K.

708 **Fig. 8** Comparisons of the electrical conductivities of the gneiss samples measured at
709 1.5 GPa in this study and in previous studies. The dashed blue and green lines
710 represent the electrical conductivities of granulite and gneiss at 1.0 GPa from Fuji-
711 ta et al. (2004) and Fuji-ta et al. (2007), respectively, the dashed orange line
712 represents the electrical conductivity of quartz at 1.0 GPa from Wang et al. (2010),
713 the dashed dark green line represents the electrical conductivity of alkali feldspars
714 at 1.0 GPa from Hu et al. (2013), the dashed sky blue line represents the electrical
715 conductivity of natural PP216 metapelite at 0.3 GPa from Hashim et al. (2013), the
716 dashed violet line represents the electrical conductivity of the residual JOY2-X4
717 enclave at 0.3 GPa from Ferri et al. (2013), the dashed red lines represent the
718 electrical conductivity of granite at 0.5 GPa from Dai et al. (2014), and the dashed

719 pink line represents the electrical conductivity of phlogopite at 1.0 GPa from Li et
720 al. (2016).
721 **Fig. 9** Geological sketch map of the Dabie-Sulu orogenic belt (a) and its correspondent
722 lithological distribution diagram in the southern counterpart of Dabie-Sulu region
723 (b) (modified after Xu et al., 2013; Liu et al., 2014).
724 **Fig. 10** Laboratory-based conductivity–depth profiles constructed from data of the
725 gneiss samples, and the thermodynamic parameters, and comparison with
726 geophysically inferred field results from Dabie–Sulu UHPM belt, China. The red
727 solid lines represent the conductivity–depth profiles based on the conductivities of
728 the samples described in Fig. 3 and based on a surface heat flow of 75 mW/m^2 in
729 Dabie–Sulu UHPM belt. The dashed blue lines represent the conductivity–depth
730 profiles based on the conductivities of eclogite, and the dashed brown line
731 represents the conductivity–depth profiles based on the conductivities of granulite
732 (Fuji-ta et al., 2004; Dai et al., 2016). The green region represents the MT data
733 derived from high conductivity anormaly in Dabie–Sulu UHPM belt (Xiao et al.,
734 2007; He et al., 2009).
735
736
737
738
739
740
741
742
743
744
745
746
747
748

Table 1. Mineralogical assemblage of three natural gneiss samples. Pl=plagioclase, Qz=quartz and Bi=biotite.

Run No.	Mineralogical associations
DS12	Pl (50%) + Qz (40%) + Bi (10%)
DS13	Pl (25%) + Qz (40%) + Bi (35%)
DS14	Pl (60%) + Qz (25%) + Bi (15%)

774 **Table 2.** Chemical composition of whole rock analysis by X-ray fluorescence (XRF) for three
775 gneiss samples.

Oxides (wt.%)	DS12	DS13	DS14
SiO_2	64.40	68.59	69.87
Al_2O_3	15.30	13.62	14.88
MgO	3.15	3.00	1.78
CaO	1.61	2.48	0.52
Na_2O	2.27	2.46	2.26
K_2O	3.24	2.33	4.86
Fe_2O_3	6.28	5.57	3.37
TiO_2	0.81	0.61	0.38
Cr_2O_3	0.02	0.02	0.01
MnO	0.08	0.07	0.03
BaO	0.06	0.02	0.12
SrO	0.03	0.03	0.02
P_2O_5	0.19	0.16	0.08
SO_3	<0.01	<0.01	0.28
L.O.I	1.89	0.86	1.67
Total	99.33	99.82	100.13

776
777
778
779
780
781
782
783
784
785
786

Table 3. Fitted parameters of the Arrhenius relation for the electrical conductivity of three gneiss samples. Two equations of $\sigma = \sigma_0 \exp(-\Delta H/kT)$ and $\Delta H = \Delta U + P\Delta V$ are adopted, in here, σ_0 is the pre-exponential factor (S/m), ΔH is the activation enthalpy (eV), k is the Boltzmann constant (eV/K), T is the absolute temperature (K), ΔU is the activation energy (eV), P is the pressure (GPa) and ΔV is the activation volume (cm^3/mole). The symbol of R^2 is denoted as the fitted correlation coefficient.

Run No.	P (GPa)	T (K)	Log σ_0 (S/m)	ΔH (eV)	R^2	ΔU (eV)	ΔV (cm^3/mole)
DS12	0.5	623–723	-0.20±0.09	0.58±0.01	99.91	0.63±0.01	-7.10±0.92
	1.0	623–723	-0.06±0.01	0.56±0.01	99.99		
	1.5	623–773	-0.06±0.02	0.52±0.02	99.66		
	2.0	623–773	-0.38±0.05	0.47±0.01	99.96		
	0.5	773–1073	1.11±0.08	0.77±0.01	99.79		
	1.0	773–1073	0.98±0.08	0.72±0.01	99.77	0.78±0.03	-2.69±2.40
	1.5	823–1073	1.43±0.05	0.76±0.01	99.93		
	2.0	823–1073	1.26±0.11	0.71±0.03	99.51		
DS13	1.5	623–773	-0.92±0.04	0.35±0.01	99.93	/	/
		823–1073	2.26±0.12	0.84±0.01	99.66		
DS14	1.5	623–773	-0.49±0.10	0.38±0.01	99.60		
		823–1073	2.63±0.10	0.87±0.02	99.81		

Figure 1

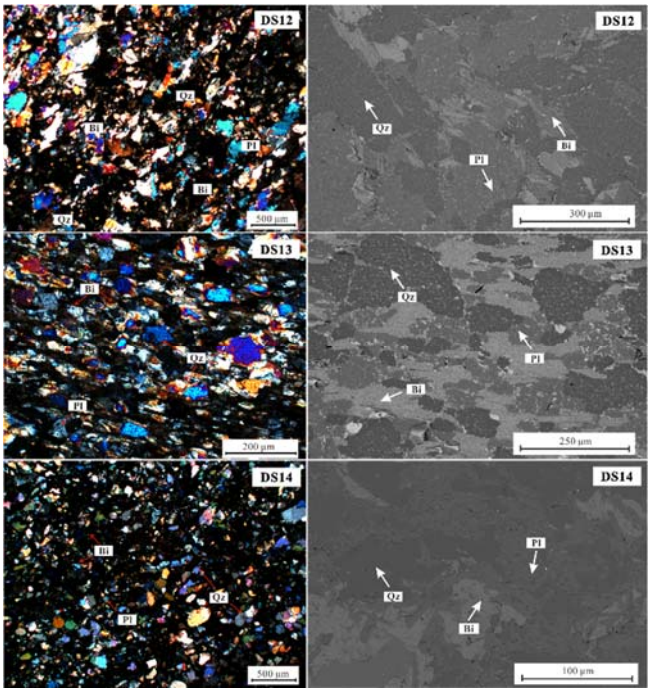
DS12
Qz
Bt
Pl
Bt
Qz
500 µm
DS12
Qz
Pl
Bt
300 µm
DS13
Bt
Qz
Pl
200 µm
DS13
Qz
Pl
Bt
250 µm
DS14
Bt
Qz
Pl
500 µm
DS14
Pl
Qz
Bt
100 µm

822 **Figure 2**

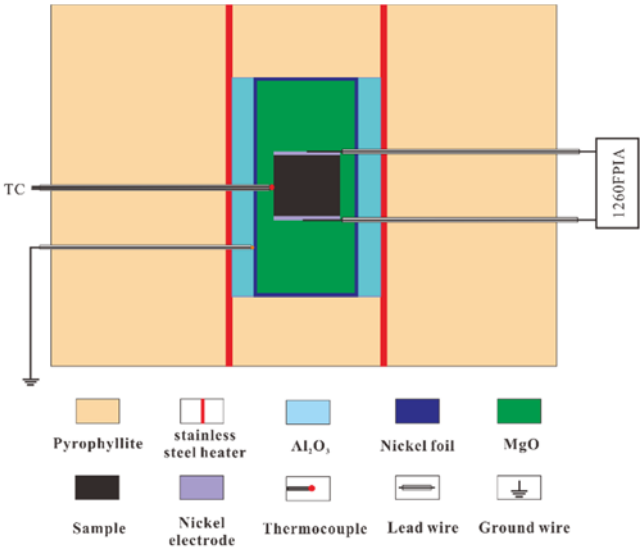

823
824
825
826
827
828
829
830
831
832
833
834
835
836
837
838
839
840
841
842

Figure 3

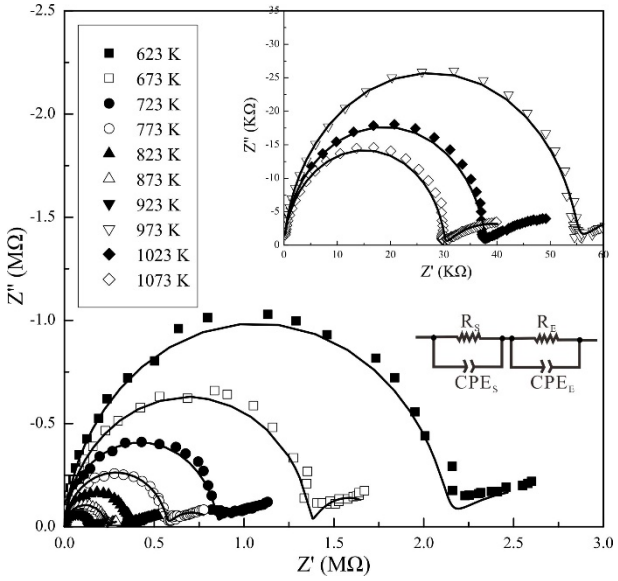
623 K
673 K
723 K
773 K
823 K
873 K
923 K
973 K
1023 K
1073 K
Z'' (MΩ)
Z' (MΩ)
Z'' (KΩ)
Z' (KΩ)
R_S
R_E
CPE_S
CPE_E

Figure 4

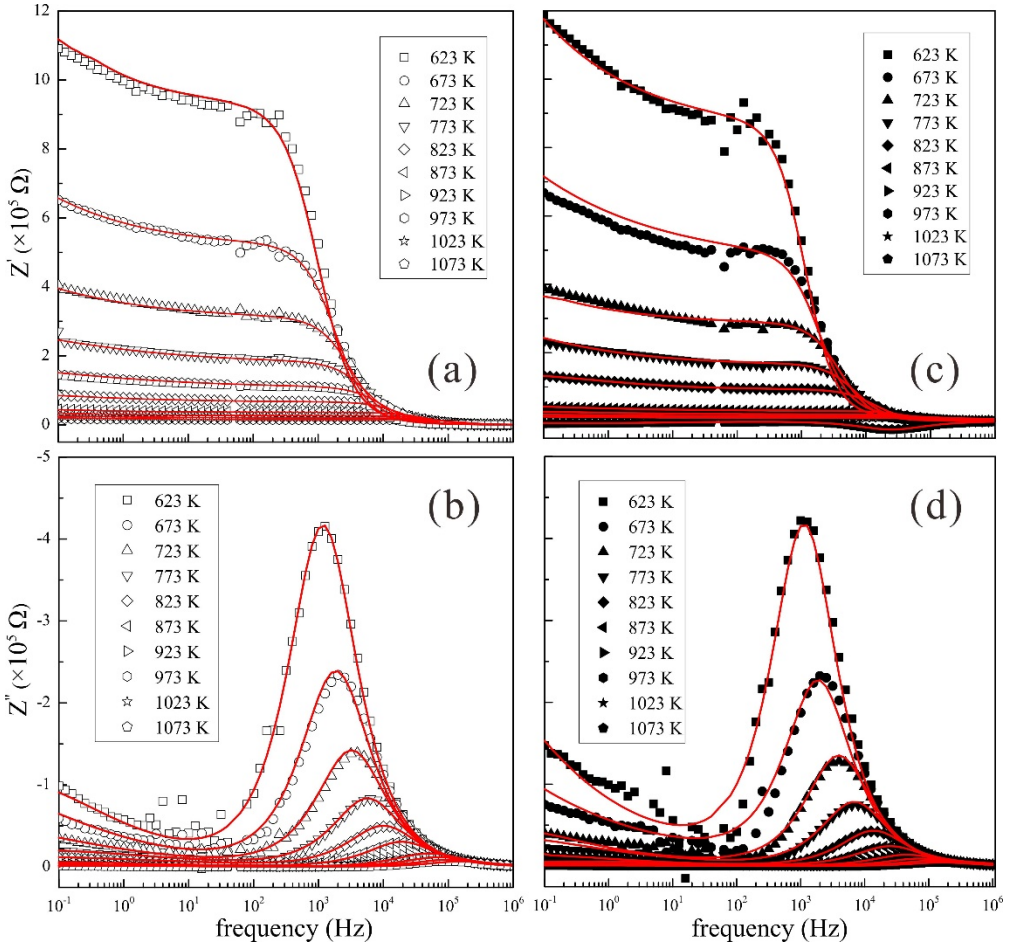
(a)
(b)
(c)
(d)
623 K
673 K
723 K
773 K
823 K
873 K
923 K
973 K
1023 K
1073 K
Z' (×10^5 Ω)
Z'' (×10^5 Ω)
frequency (Hz)
frequency (Hz)

Figure 5

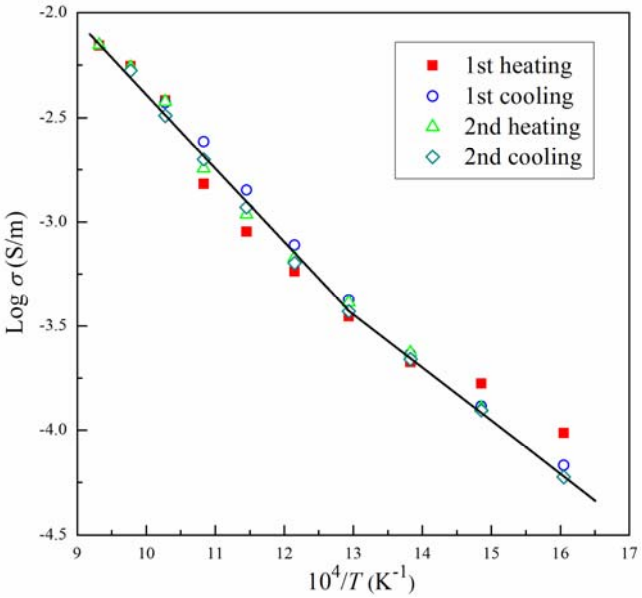
1st heating
1st cooling
2nd heating
2nd cooling
Log σ (S/m)
$10^4/T$ (K^{-1})
-2.0
-2.5
-3.0
-3.5
-4.0
-4.5
9
10
11
12
13
14
15
16
17

Figure 6

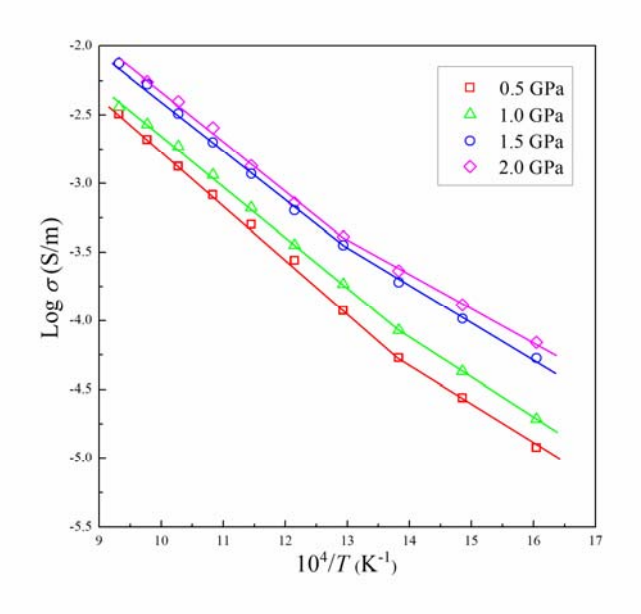
0.5 GPa
1.0 GPa
1.5 GPa
2.0 GPa
Log σ (S/m)
10⁴/T (K⁻¹)
-2.0
-2.5
-3.0
-3.5
-4.0
-4.5
-5.0
-5.5
9
10
11
12
13
14
15
16
17

Figure 7

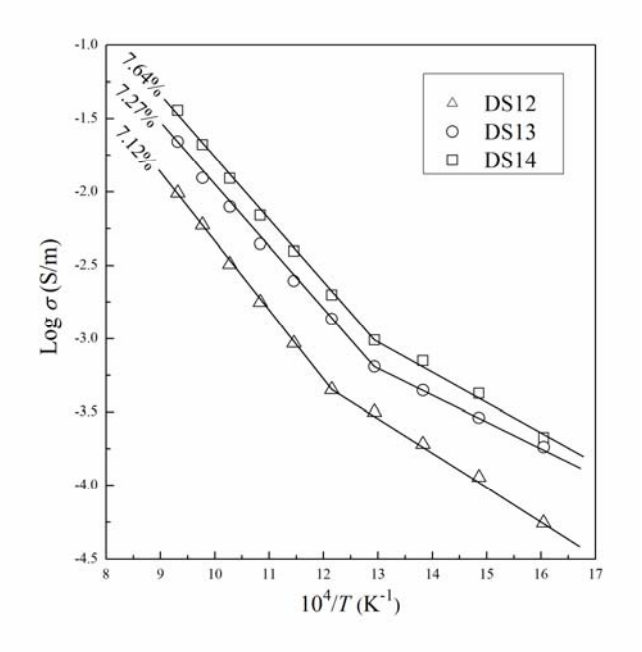

Figure 8

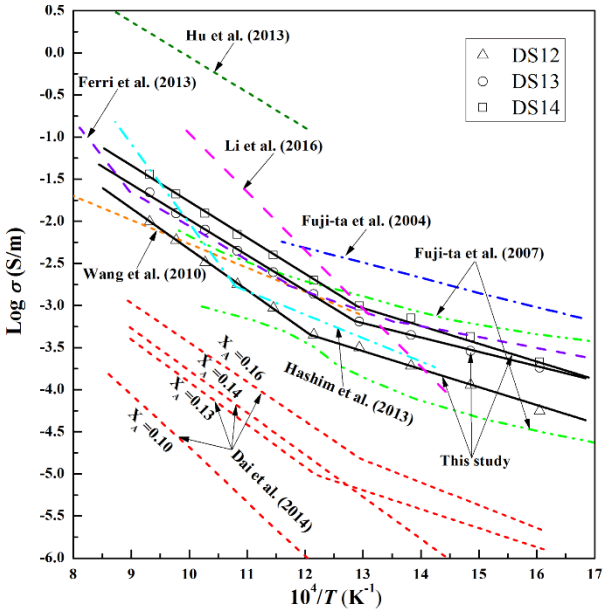
Hu et al. (2013)
Ferri et al. (2013)
Li et al. (2016)
Fuji-ta et al. (2004)
Fuji-ta et al. (2007)
Wang et al. (2010)
Hashim et al. (2013)
This study
Dai et al. (2014)
DS12
DS13
DS14
X_A=0.16
X_A=0.14
X_A=0.13
X_A=0.10
Log σ (S/m)
$10^4/T$ (K^{-1})

Figure 9

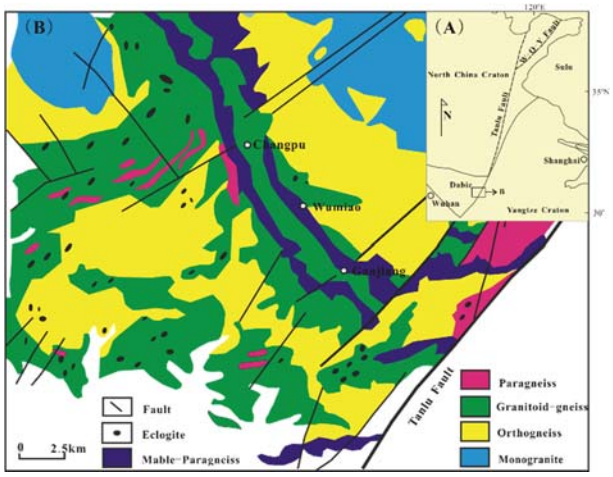
(B)
(A)
Changpu
Wumiao
Guanhang
Tanlu Fault
Fault
Eclogite
Mable–Paragneiss
0 2.5km
Paragneiss
Granitoid–gneiss
Orthogneiss
Monogranite
North China Craton
Sulu
Shanghai
Dabie
Yangtze Craton

985 **Figure 10**

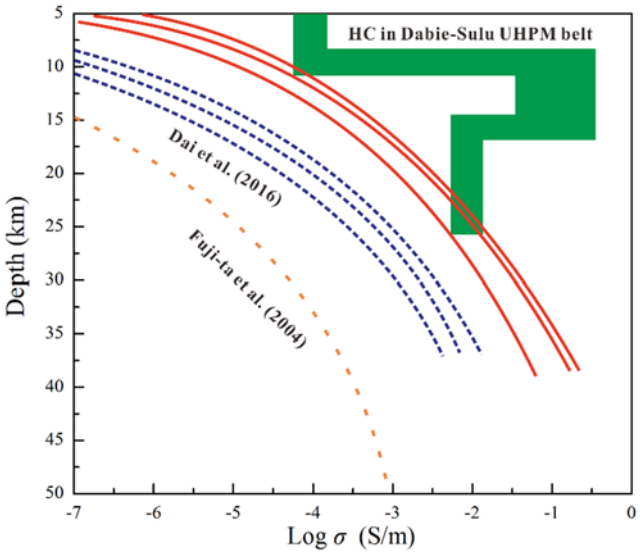

986